

Huygens Principle Based Imaging of Multilayered Objects with Inclusions

Navid Ghavami^{1, *}, Gianluigi Tiberi^{2, 4}, David J. Edwards¹,
Ahmad Safaai-Jazi³, and Agostino Monorchio⁴

Abstract—The application of a recently introduced microwave imaging technique based on the Huygens principle (HP), has been extended to multilayered objects with inclusions in this paper. The methodology of HP permits the capture of contrast such that different material properties within the region of interest can be discriminated in the final image, and its simplicity removes the need to solve inverse problems when forward propagating the waves. Therefore the procedure can identify and localize significant scatterers inside a multilayered volume, without having apriori knowledge on the dielectric properties of the target object. Additionally, an analytically-based approach for analyzing UltraWide Bandwidth (UWB) body propagation is presented, where the body is modeled as a 3-layer stratified cylinder with an eccentric inclusion. Validation of the technique through both simulations and measurements on multilayered cylindrical objects with inclusions has been performed.

1. INTRODUCTION

Microwave imaging is an attractive and promising non-ionizing imaging modality for medical applications. An increasing number of research groups investigate its applicability to breast cancer detection, which is motivated by the significant contrast in the dielectric properties of normal and malignant tissues at microwave frequencies.

At present, there are two main breast imaging techniques employing microwave signals: microwave tomography [1–8] and UWB radar techniques [9–13]. Microwave tomography techniques permit dielectric properties reconstruction by solving non linear inverse scattering problems, while UWB radar techniques solve simpler computational problems by seeking only to identify the significant scatterers inside the target volume. However, UWB radar techniques may encounter difficulties in imaging spaces which possess volumes of varying dielectric constant.

Here, we will describe the extension of a recently introduced UWB microwave imaging technique based on the Huygens Principle [14] for treating multilayered objects with inclusions. More in detail, we will first investigate analytically the propagation phenomena of UWB signal in human-like tissues (in contrast to conventional approaches based on Finite Difference Time Domain-FDTD methods); specifically, the body will be modeled as a 3-layer eccentric cylinder of infinite length, and Maxwell's equations will be solved. Next, the UWB microwave imaging method introduced in [14] will be employed using both the analytical results and measurements obtained on appropriate phantoms. As stated earlier, the method is based on the Huygens Principle; using HP to forward propagate the waves removes the need to solve inverse problems, which in turn, removes the need for matrix generation/inversion. Furthermore, UWB allows the utilization of all the information in the frequency domain by combining the information from the individual frequencies, resulting in the construction of a consistent image. It

Received 10 December 2013, Accepted 7 February 2014, Scheduled 11 February 2014

* Corresponding author: Navid Ghavami (navid.ghavami@eng.ox.ac.uk).

¹ Department of Engineering Science, University of Oxford, Parks Road, Oxford, UK. ² Fondazione Imago7, Viale del Tirreno, Pisa I-56128, Italy. ³ Department of Electrical and Computer Engineering, Virginia Tech University, US. ⁴ Department of Information Engineering, University of Pisa, Via G. Caruso 16, Pisa I-56122, Italy.

follows that the methodology can identify the presence and location of significant scatterers inside a multilayered volume without having apriori knowledge on the dielectric properties of the target object.

Previously, the authors have performed successful simulation and measurement tests to validate the HP on canonical objects with single and multiple eccentric inclusions [14–16]. In this paper, stratified cylinders involving at least 3 different layers are used as models in both simulations and measurements. Potential applications of this method include breast cancer detection, internal organ imaging, and whole body imaging.

The paper is organized as follows. In Section 2, Maxwell's equations are solved for a 3-layer stratified eccentric cylinder model. In Section 3, the HP based procedure is reviewed, and the procedure is verified through realistic simulations in Section 4. Validation of the method through measurements on a multi-layered cylinder is given in Section 4, and finally Section 5 concludes the paper.

2. 3-LAYER STRATIFIED ECCENTRIC CYLINDER

Scattering by cylindrical objects, for both concentric and eccentric cases, has been previously investigated by other researchers [17–19]. Here, we consider a 3-layer stratified cylinder in free space, illuminated by a plane wave having a frequency f , with TM -polarization and normal incidence with respect to the z -axis. Moreover, a time-harmonic phasor notation will be used in the entire paper. The three cylinders are indicated as cylinder '0', cylinder '1' and cylinder '2', and have radiuses a_0 , a_1 and a_2 respectively (see Fig. 1).

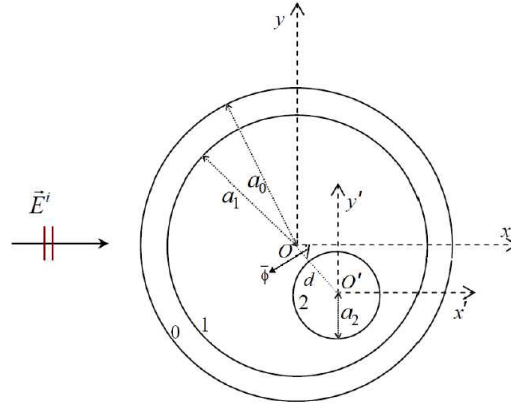


Figure 1. 3-layer stratified eccentric cylinder in free space.

Cylinder '0' is characterized by ε_1 , μ_1 , both of which can be complex and can vary with the frequency. Thus we have:

$$k_1 = \omega \sqrt{\varepsilon_1 \mu_1}, \quad \omega = 2\pi f \quad (1a)$$

$$Z_1 = \sqrt{\frac{\mu_1}{\varepsilon_1}} \quad (1b)$$

Cylinder '1' is characterized by ε_2 , μ_2 , both of which can be complex and can vary with the frequency. It holds:

$$k_2 = \omega \sqrt{\varepsilon_2 \mu_2} \quad (2a)$$

$$Z_2 = \sqrt{\frac{\mu_2}{\varepsilon_2}} \quad (2b)$$

Cylinder '2' is characterized by ε_3 , μ_3 , both of which can be complex and can vary with the frequency. Such that:

$$k_3 = \omega \sqrt{\varepsilon_3 \mu_3} \quad (3a)$$

$$Z_3 = \sqrt{\frac{\mu_3}{\varepsilon_3}} \quad (3b)$$

To determine the field in different regions, we start by writing the field expressions for axial components, where ϕ_0 represents the angle of incidence of the plane wave.

$$E_z^0 = E_0 \sum_{n=-\infty}^{+\infty} (-j)^n \left[J_n(k_0\rho) + o_{0,n}H_n^{(2)}(k_0\rho) \right] e^{jn(\phi-\phi_0)}, \quad \rho > a_0 \quad (4a)$$

$$E_z^1 = E_0 \sum_{n=-\infty}^{+\infty} (-j)^n \left[i_{1,n}J_n(k_1\rho) + o_{1,n}H_n^{(2)}(k_1\rho) \right] e^{jn\phi}, \quad a_1 < \rho < a_0 \quad (4b)$$

$$E_z^2 = E_0 \sum_{n=-\infty}^{+\infty} (-j)^n \left[i_{2,n}J_n(k_2\rho') + o_{2,n}H_n^{(2)}(k_2\rho') \right] e^{jn\phi'}, \quad \rho < a_1 \text{ and } \rho' > a_2 \quad (4c)$$

$$E_z^3 = E_0 \sum_{n=-\infty}^{+\infty} (-j)^n i_{3,n}J_n(k_3\rho') e^{jn\phi'}, \quad \rho' < a_2 \quad (4d)$$

Equation (4) hold in free-space, inside cylinder '0', inside cylinder '1' and inside cylinder '2', respectively. It should be pointed out that the *primes* just after Hankel and Bessel functions indicate differentiation with respect to the argument, while the other *primes* denote the eccentrically displaced coordinate system. Similarly we have the following field expressions for azimuthal components:

$$H_\phi^0 = \frac{E_0}{jZ_0} \sum_{n=-\infty}^{+\infty} (-j)^n \left[J'_n(k_0\rho) + o_{0,n}H'_n{}^{(2)}(k_0\rho) \right] e^{jn(\phi-\phi_0)}, \quad \rho > a_0 \quad (5a)$$

$$H_\phi^1 = \frac{E_0}{jZ_1} \sum_{n=-\infty}^{+\infty} (-j)^n \left[i_{1,n}J'_n(k_1\rho) + o_{1,n}H'_n{}^{(2)}(k_1\rho) \right] e^{jn\phi}, \quad a_1 < \rho < a_0 \quad (5b)$$

$$H_{\phi'}^2 = \frac{E_0}{jZ_2} \sum_{n=-\infty}^{+\infty} (-j)^n \left[i_{2,n}J'_n(k_2\rho') + o_{2,n}H'_n{}^{(2)}(k_2\rho') \right] e^{jn\phi'}, \quad \rho < a_1 \text{ and } \rho' > a_2 \quad (5c)$$

$$H_{\phi'}^3 = \frac{E_0}{jZ_3} \sum_{n=-\infty}^{+\infty} (-j)^n i_{3,n}J'_n(k_3\rho') e^{jn\phi'}, \quad \rho' < a_2 \quad (5d)$$

By applying the boundary condition at $\rho = a_0$ we have:

$$\begin{aligned} E_z^0(\rho = a_0) &= E_z^1(\rho = a_0) \\ \Rightarrow \left[J_n(k_0a_0) + o_{0,n}H_n^{(2)}(k_0a_0) \right] e^{-jn\phi_0} &= i_{1,n}J_n(k_1a_0) + o_{1,n}H_n^{(2)}(k_1a_0) \end{aligned} \quad (6a)$$

$$\begin{aligned} H_\phi^0(\rho = a_0) &= H_\phi^1(\rho = a_0) \\ \Rightarrow \left[J'_n(k_0a_0) + o_{0,n}H'_n{}^{(2)}(k_0a_0) \right] e^{-jn\phi_0} &= \frac{Z_0}{Z_1} \left[i_{1,n}J'_n(k_1a_0) + o_{1,n}H'_n{}^{(2)}(k_1a_0) \right] \end{aligned} \quad (6b)$$

From (6a) and (6b),

$$i_{1,n} = R_n + o_{0,n}S_n \quad (7a)$$

$$o_{1,n} = \bar{R}_n + o_{0,n}\bar{S}_n \quad (7b)$$

where, R_n , S_n , \bar{R}_n and \bar{S}_n are calculated after solving system of (6a) and (6b).

Next, applying the boundary condition at $\rho' = a_2$ we have:

$$E_z^2(\rho' = a_2) = E_z^3(\rho' = a_2) \Rightarrow i_{2,n}J_n(k_2a_2) + o_{2,n}H_n^{(2)}(k_2a_2) = i_{3,n}J_n(k_3a_2) \quad (8a)$$

$$H_{\phi'}^2(\rho' = a_2) = H_{\phi'}^3(\rho' = a_2) \Rightarrow i_{2,n}J'_n(k_2a_2) + o_{2,n}H'_n{}^{(2)}(k_2a_2) = \frac{Z_2}{Z_3} i_{3,n}J'_n(k_3a_2) \quad (8b)$$

From (8a) and (8b),

$$o_{2,n} = -i_{2,n}Q_n \quad (9)$$

where Q_n can be determined by manipulating (8). To facilitate the imposition of boundary conditions at $\rho = a_1$, E_z^2 and H_ϕ^2 are first expressed in terms of ρ and ϕ [20].

$$E_z^2 = E_0 \sum_{n=-\infty}^{+\infty} (-j)^n \left[i_{2,n} \sum_{m=-\infty}^{+\infty} J_{m-n}(k_2 d) J_m(k_2 \rho) e^{jm\phi} e^{-j(m-n)\bar{\phi}} + o_{2,n} \sum_{m=-\infty}^{+\infty} H_m^{(2)}(k_2 \rho) J_{m-n}(k_2 d) e^{jm\phi} e^{-j(m-n)\bar{\phi}} \right], \quad \rho < a_1 \text{ and } \rho' > a_2 \quad (10a)$$

$$H_\phi^2 = \frac{E_0}{jZ_2} \sum_{n=-\infty}^{+\infty} (-j)^n E_0 \left[i_{2,n} \sum_{m=-\infty}^{+\infty} J_{m-n}(k_2 d) J'_m(k_2 \rho) e^{jm\phi} e^{-j(m-n)\bar{\phi}} + o_{2,n} \sum_{m=-\infty}^{+\infty} H'_m{}^{(2)}(k_2 \rho) J_{m-n}(k_2 d) e^{jm\phi} e^{-j(m-n)\bar{\phi}} \right], \quad \rho < a_1 \text{ and } \rho' > a_2 \quad (10b)$$

In above, d and $\bar{\phi}$ represent the distance between the axes of cylinders '1' and '2' (OO') and the angle between OO' and x -axis, respectively.

Moving on to the boundary condition at $\rho = a_1$, we have:

$$\begin{aligned} E_z^1(\rho = a_1) &= E_z^2(\rho = a_1) \Rightarrow \sum_{n=-\infty}^{+\infty} (-j)^n \left[i_{1,n} J_n(k_1 a_1) + o_{1,n} H_n^{(2)}(k_1 a_1) \right] e^{jn\phi} \\ &= \sum_{n=-\infty}^{+\infty} (-j)^n \left[i_{2,n} \sum_{m=-\infty}^{+\infty} J_{m-n}(k_2 d) J_m(k_2 a_1) e^{jm\phi} e^{-j(m-n)\bar{\phi}} + o_{2,n} \sum_{m=-\infty}^{+\infty} H_m^{(2)}(k_2 a_1) J_{m-n}(k_2 d) e^{jm\phi} e^{-j(m-n)\bar{\phi}} \right] \end{aligned} \quad (11a)$$

$$\begin{aligned} H_\phi^1(\rho = a_1) &= H_\phi^2(\rho = a_1) \Rightarrow \sum_{n=-\infty}^{+\infty} (-j)^n \left[i_{1,n} J'_n(k_1 a_1) + o_{1,n} H'_n{}^{(2)}(k_1 a_1) \right] e^{jn\phi} \\ &= \frac{Z_1}{Z_2} \sum_{n=-\infty}^{+\infty} (-j)^n \left[i_{2,n} \sum_{m=-\infty}^{+\infty} J_{m-n}(k_2 d) J'_m(k_2 a_1) e^{jm\phi} e^{-j(m-n)\bar{\phi}} + o_{2,n} \sum_{m=-\infty}^{+\infty} H'_m{}^{(2)}(k_2 a_1) J_{m-n}(k_2 d) e^{jm\phi} e^{-j(m-n)\bar{\phi}} \right] \end{aligned} \quad (11b)$$

Employing the orthogonality property of $e^{-jl\phi}$ ($\int_0^{2\pi} e^{-jl\phi} e^{jm\phi} d\phi = 2\pi$ if $l = m$ and $= 0$ if $l \neq m$), and after some Algebraic manipulation the following result is obtained,

$$\sum_{n=-\infty}^{+\infty} i_{2,n} G_{l,n} = V_l \quad (12)$$

where $G_{l,n}$ and V_l can be determined by manipulating (11). Equation (12) is represented through a summation with n spanning from $-\infty$ to $+\infty$. For computation, the summation is truncated after $2N + 1$ terms, i.e., with n going from $-N$ to $+N$. N has to be set so that convergence is achieved (i.e., relative error lower than 3%), which depends on the frequency and the radius a_0 . For the work here we have used $N = 15$.

Thus, all inward and outward fields, and hence the field everywhere inside the stratified cylinder have been calculated. It should be noted that if the cylinder (Fig. 1) is illuminated by an electrical z -directed line source of intensity I , then all the expressions in this section which have been derived from the plane wave illumination can still be used by simply replacing $(-j)^n$ with $H_n^{(2)}(k_0 \rho_0)$, where ρ_0 represents the distance of the line source from the axis of the cylinder.

3. THE HUYGENS PRINCIPLE-BASED PROCEDURE

In this section, we briefly recall the HP based procedure, presented in [14], inserting some parts of [14] to help the reader in following and understanding the paper. Let us consider a cylinder with a radius a_0 in free space. The cylinder is illuminated by a transmitting line source tx_m and operates at a frequency f . At this point, it is assumed that the dielectric properties of the cylinder, i.e., the dielectric constant ϵ_{r1} and the conductivity σ_1 are known. As an inclusion, a smaller cylinder with a higher dielectric constant than ϵ_{r1} is placed inside the original cylinder (Fig. 2). The problem consists of identifying the presence and location of the inclusion by using only the fields measured outside the cylinder.

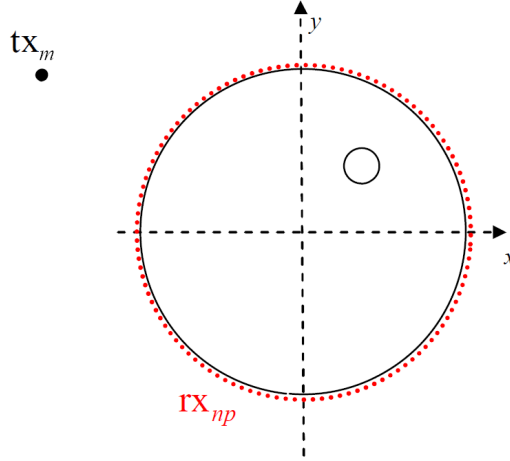


Figure 2. Pictorial view of the problem.

Suppose that the field at the surface points $rx_{np} = (a_0, \phi_{np})$ is known, such that:

$$E|_{rx_{np}} = E_{np} \quad \text{with} \quad np = 1, \dots, N_{PT} \quad (13)$$

where N_{PT} indicates the number of measured points across the outside cylinder. We calculate the field inside the cylinder as the superposition of the fields radiated by the N_{PT} observation points of (13):

$$E_{HP}^{rcstr}(\rho, \phi; tx; f) = \Delta_s \sum_{np=1}^{N_{PT}} E_{np} G(k_1 |\vec{\rho}_{np} - \vec{\rho}|) \quad (14)$$

where $G(k_1 |\vec{\rho}_{np} - \vec{\rho}|)$ is the Green's function defined in [14], $(\rho, \phi) \equiv \vec{\rho}$ the observation point, k_1 the wave number for the media constituting the cylinder, and Δ_s the spatial sampling value. In (14), the string "rcstr" is used to indicate the reconstructed internal field, while the string HP indicates that a HP-based procedure will be employed. Thus, assuming we have M transmitting sources tx_m with $m = 1, 2, \dots, M$, and N_F frequencies f_i , the intensity of the resulting image I using the Green's functions can be obtained through:

$$I_{HP}(\rho, \phi) = \frac{1}{B} \sum_{m=1}^M \sum_{i=1}^{N_F} \Delta_f |E_{HP}^{rcstr}(\rho, \phi; tx; f_i)|^2 \quad (15)$$

In (15), Δ_f and B represent the frequency and the bandwidth, respectively.

During the initial simulations, it was observed that an image of the transmitter appeared in the result, which sometimes masked the area of interest. However, this transmitter image can be successfully removed by modifying (14) such that:

$$E_{HP}^{rcstr}(\rho, \phi; tx; f) = \Delta_s \sum_{np=1}^{N_{PT}} (E_{np} - \text{avg}_M\{E_{np}\}) G(k_1 |\vec{\rho}_{np} - \vec{\rho}|) \quad (16)$$

where $\text{avg}_M\{E_{np}\}$ represents the average of signals obtained illuminating the object using M different transmitter positions. This in effect "smears" out the transmitter image.

4. VALIDATION THROUGH SIMULATION: MULTILAYERED OBJECT WITH AN ECCENTRIC INCLUSION

Before proceeding to perform an experiment, the applicability of the analytical formulation was tested by simulating a 3-layer cylindrical object with an eccentric inclusion. To verify this using the HP procedure, an external Agar cylinder in free space having a radius of 4.25 cm, with electrical properties (frequency independent for the moment) of $\varepsilon_{r1} = 70$ and $\sigma_1 = 0.5 \text{ S/m}$, with inclusions is considered. A smaller cylinder of radius 3 cm, with the same dielectric constant value but a higher conductivity value $\sigma_1 = 2 \text{ S/m}$ is placed inside the outer cylinder to represent the second medium. Finally, an eccentric inclusion made of a Perfectly Electrically Conducting (PEC) cylinder of radius 3 mm, is placed 1.75 cm away from the axis of the cylinder, 90° degrees relative to the x -axis.

The external cylinder is illuminated using 4 transmitter sources situated 8 cm from the axis of the cylinder, while a frequency band of 1–3 GHz with frequency spacing of 10 MHz is used. For each illuminating source and for each frequency, the field (E_{np}) at $N_{PT} = 120$ points lying on the external surface is calculated. It should be noted that in this example, E_{np} has been determined using the analysis presented in Section 2. Finally, the average of the 4 data sets ($\text{avg}_M\{E_{np}\}$) is calculated and the Huygens principle is applied to the difference between the measured field and the average field as stated in (16). Fig. 3 shows the normalized intensity obtained through (15) and using an appropriate image adjusting. The image is adjusted by enforcing to zero the intensity values below 0.5 and expanding from 0 to 1 of the values above 0.5. A peak can be clearly detected in the regions of the inclusions: thus, both detection and localization are achieved for this multi-layered problem.

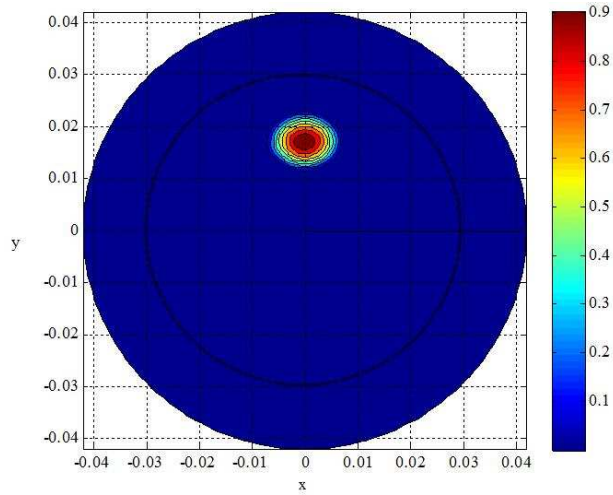


Figure 3. Cylinder with an inclusion: normalized intensity obtained through (15). All scales are in meters.

Next, a similar geometrical model, this time with realistic human body tissue properties assigned to its three layers is further simulated. The external cylinder is assumed to be a thin human skin with radius 4.25 cm, $\varepsilon_{r1} = 41$ and $\sigma_1 = 0.8 \text{ S/m}$ [21]. The internal concentric cylinder and the eccentric inclusion are then assigned the electrical properties of a normal ($\varepsilon_{r1} = 10$ and $\sigma_1 = 0.8 \text{ S/m}$) and malignant ($\varepsilon_{r1} = 50$ and $\sigma_1 = 1 \text{ S/m}$) tissue respectively. In the simulation, the radius of the middle cylinder is increased to 4.05 cm in order to have a thin skin layer of only 2 mm, while the sizes of other layers remain unchanged. The same frequency range, sampling and transmitting sources and other conditions as the previous simulation are implemented here. Fig. 4(b) shows the normalized intensity obtained through (15) and using an appropriate image adjusting and averaging. It is important to point out that in this simulation, the quantity k_2 is used instead of k_1 in the Green's function for the reconstruction process. This is due to the fact that as a thin skin layer is used to represent the outer layer, the target is now contained in the second layer, which represents a normal breast tissue.

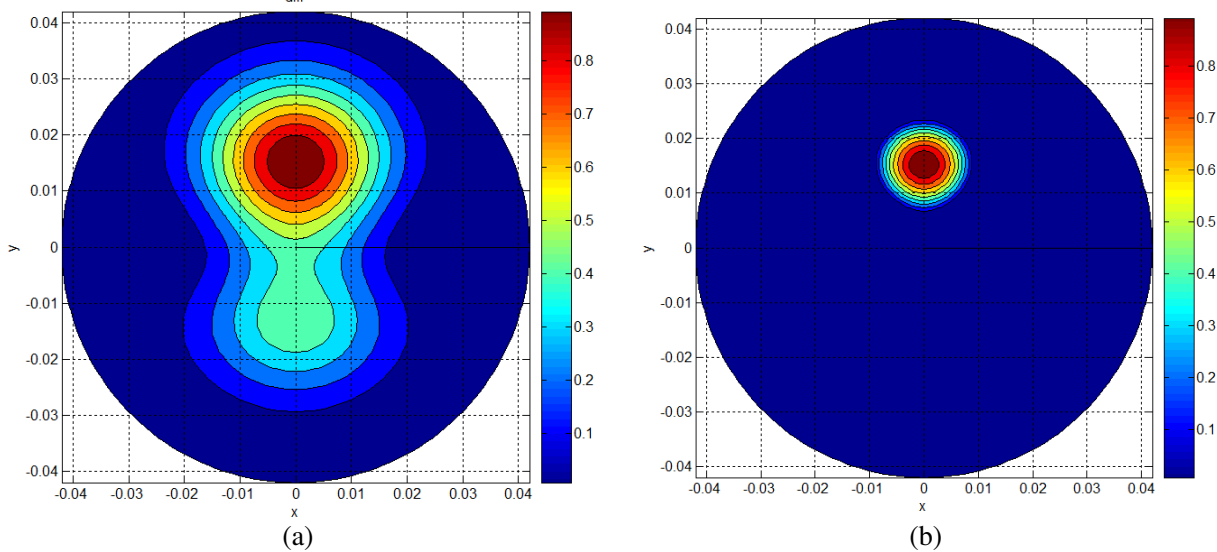


Figure 4. Normalized intensity obtained through (15), (a) before image adjusting, (b) after image adjusting. All scales are in meters.

A peak can be clearly detected in the region of the inclusion. It can be seen that the method successfully detects and locates the breast tumor in this multilayered simulation, and knowing that malignant breast tissue has a conductivity value higher than most human tissues [22], its detection will be achieved in nearly all cases.

Next, an analysis of the signal to clutter ratio and resolution with respect to the band is performed. Specifically, We define the signal to clutter ratio (S/C) as the ratio between the maximum inclusion response and the maximum clutter response in the same image [10]. To evaluate the S/C with respect to the band, we apply (15) for different bandwidths; more in detail, we perform image reconstruction assuming a bandwidth of 1, 2, and 4 GHz (the lower frequency is fixed at 1 GHz). Next, for each image the S/C is calculated and reported in Table 1. Note that in HP procedure the within-breast S/C approaches 4 dB for a bandwidth of 4 GHz. This value has been obtained with $M = 4$ transmitter positions, $N_{PT} = 120$, and a frequency sampling of 20 MHz. The reader is invited to refer to [14] for further detail concerning variation of S/C with respect to M , N_{PT} and frequency sampling. In the same paper, it has been shown that an increase of approximately 4 dB occurs if using $M = 12$. Note that in [10], for a similar problem of 4 GHz bandwidth, a within-breast S/C of 4.1 dB has been obtained by employing the delay-and-sum beamforming algorithm and using $M = 45$, while in [23] a within-breast S/C of 4 dB has been obtained by employing time reversal approach and using $M = 7$. Note that in both [10] and [23], the skin has also been considered.

Table 1. Within-breast S/C and Resolution for bandwidth of 1, 2, 4 GHz.

Band (GHz)	Within-breast S/C (dB)	Resolution (mm)
1	3	7.5
2	3.5	6
4	3.9	5

Resolution, i.e., the dimension of the region whose normalized intensity is above 0.5, has been addressed with respect to the band. Specifically, in the same Table 1 the resolution is given assuming a bandwidth of 1, 2 and 4, respectively. It can be shown (see Table 1) that the resolution achieves the optical resolution limit of $\lambda_{f_{\max}}/4$; this value is better than that achieved by time reversal approach [23] and comparable to that achieved by the delay-and-sum beamforming algorithm [10]. A detailed analysis on computational time can be found in [14].

5. VALIDATION THROUGH MEASUREMENTS: MULTILAYERED OBJECT WITH AN ECCENTRIC INCLUSION

To access the practical ability of the HP method in locating an eccentric inclusion in a multi-layered medium, a human tissue like model was constructed. To achieve this purpose, a 2 mm thick PVC cylindrical pipe with radius of 5 cm was concentrically placed inside a larger plastic pipe, also 2 mm thick but with a larger radius of 6.25 cm. Both pipes were filled with agar-agar gel approximating a high water-content human tissue; a 3 mm thick PEC rod representing a tumor was positioned eccentrically inside the gel [Fig. 5(a)], at a distance of 3.25 cm from the axis of the cylinders [Fig. 5(b)]. Although the thickness of the pipes was chosen to be as narrow as possible (2 mm), their minimal effect on the imaging procedure could not be ignored, making this model effectively a 5-layered problem.

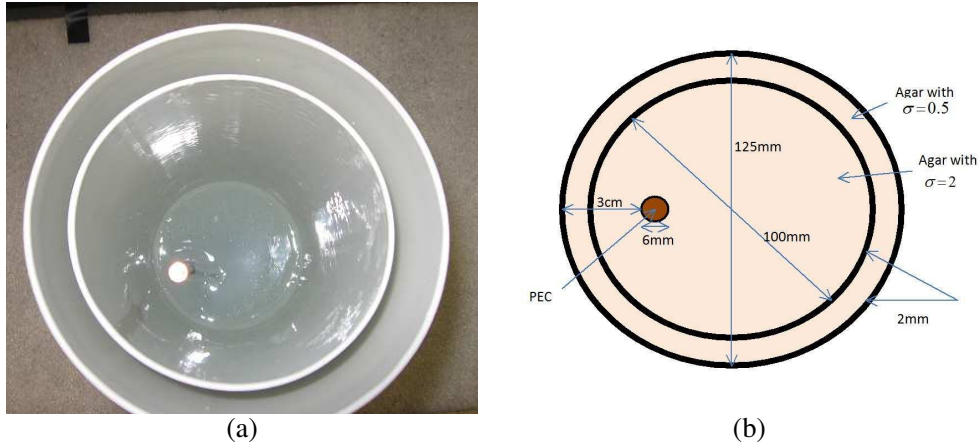


Figure 5. (a) Multilayered medium with an inclusion, (b) pictorial view of the problem.

The agar-agar was dissolved in hot water at approximately 95°C and then cooled to room temperature to form a semi-transparent jell. The dielectric constant and the conductivity are functions of the concentration of the agar-agar [24]; for this experiment two distinct concentrations of Agar were used. The external plastic pipe was filled with a lower conductive Agar ($\sigma_1 = 0.5$), while the smaller plastic pipe was filled with a higher conductive Agar ($\sigma_1 = 2$). This increase in conductivity value was gained by adding the necessary amount of salt to the original Agar mixture, whilst the change in the dielectric constant value was not notable and was considered to be equal to 70 for both agar solutions. By comparing these values with those given in [22], it can be noted that the dielectric constant and the conductivity of agar-agar are similar to the actual dielectric properties of human tissues. It is worthwhile to point out that the loss-tangent of the agar-agar is even greater than that encountered in some human tissue imaging problems; thus, it follows that the example here presented can be considered representative of lossy media imaging problems.

Frequency-domain UWB measurements were performed in free-space, using a Vector Network Analyzer (VNA) arrangement to obtain the transfer function. Discone antennas, vertically polarized and omni-directional in the azimuth plane were used, after calibration. In order to observe the variation of signal in different frequencies, the measurements were recorded using a large frequency range of 1–10 GHz, using a frequency step of 5.6 MHz. For each set of measurements, the location of the transmitting antenna was fixed at approximately 15 cm away from the axis of the cylinder, while the receiver antenna was positioned roughly 1 cm away from the external surface of the agar-agar cylinder and mounted on a computer-controlled rotating stage with 3 degrees of angular resolution. In addition, a 30 dB amplifier was used to increase the received signal.

Next, the field E_{np} at $N_{PT} = 120$ equally ϕ -spaced points lying on the external surface was measured; it should be noted that the employed number of points leads to a spatial sampling of approximately $0.1\lambda_{1,f_{\max}}$, where $\lambda_{1,f_{\max}}$ represents the wavelength in the P.M.M.A cylinder calculated

at the highest frequency (10 GHz). It has been shown that the number of measured points and the frequency samples can be reduced without decreasing the detection capability [15]. Four sets of data were recorded, changing the position of the transmitting antenna along ϕ with a step of 90 degrees. Next, the average of the 4 data sets ($\text{avg}_M\{E_{np}\}$) is calculated and the Huygens principle is applied to the difference between the measured field and the average field as stated in (16). However, when applying the Green's function in the reconstruction process, k_0 is now used. This is done due to the fact that the cylinder containing the target was placed in free-space and the receiving antenna was not completing touching the measurement grid, and hence the initial use of k_1 resulted in some distortion. It was then observed that the use of k_0 not only resulted in detection of the target, but also excellent positioning. Furthermore, the use of k_0 removes the need of having any knowledge about the dielectric properties of the target volume. Fig. 6(b) shows the normalized intensity obtained through (15) and using an appropriate image adjusting. The image is adjusted by enforcing to zero the intensity values below 0.5 and expanding from 0 to 1 of the values above 0.5. A peak can be clearly detected in the region of the inclusion: thus, both detection and localization are achieved for this multi-layered problem.

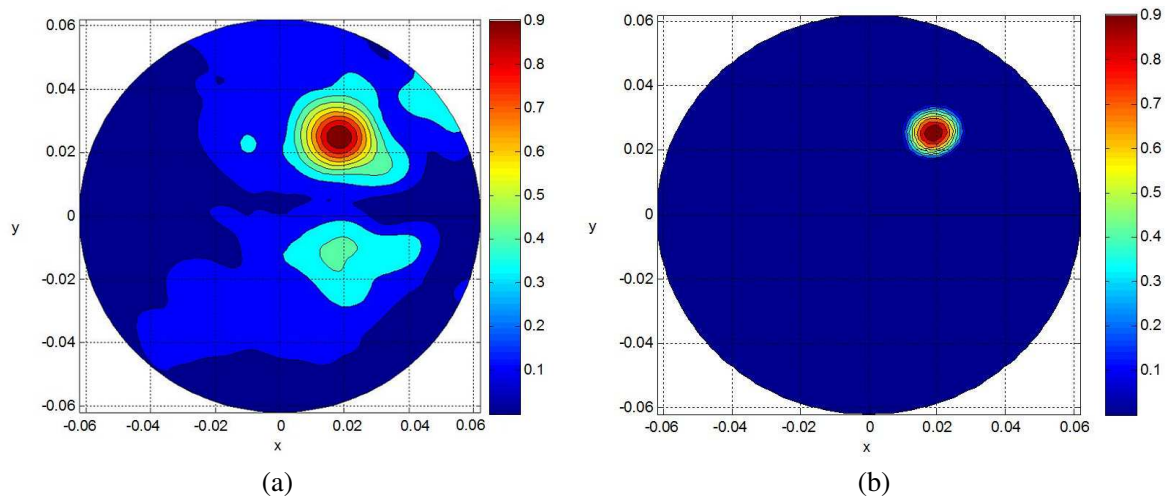


Figure 6. Normalized intensity obtained through (15), (a) before image adjusting, (b) after image adjusting. All scales are in meters.

6. CONCLUSIONS

In this paper, the analysis of a novel microwave imaging procedure based on Huygens principle has been extended to multilayered mediums. Specifically, an analytical process based on the exact Maxwell solution for a multi-layered eccentric cylinder has been formulated. The model assumes that the body can be approximated as a stratified multi-layered cylinder with an eccentric inclusion representing a tumor. The analytical model has been used for verifying HP procedure through simulations. Analyzing the S/C and the resolution of the simulated model shows that HP method provides better performance when compared to conventional time-domain approaches. Additionally, the HP has been tested through measurements using a multilayered phantom constituting of human-like tissues containing an inclusion. It has been shown that the HP can detect and locate an inclusion in multilayered cylindrical mediums. Measurements are currently being carried out on a commercial 3D inhomogeneous breast phantom with many inclusions, to further move towards solving more realistic medical imaging problems.

ACKNOWLEDGMENT

This research was partially supported by the UK Engineering and Physical Sciences Research Council and partially supported by a Marie Curie Intra European Fellowship within the 7th European Community Framework Program.

REFERENCES

1. Meaney, P. M. and K. D. Paulsen, "Nonactive antenna compensation for fixed-array microwave imaging: Part II Imaging results," *IEEE Trans. Med. Imag.*, Vol. 18, No. 6, 508–518, Jun. 1999.
2. Winters, D. W., B. D. Van Veen, and S. C. Hagness, "A sparsity regularization approach to the electromagnetic inverse scattering problem," *IEEE Transactions on Antennas and Propagation*, Vol. 58, No. 1, 145–154, Jan. 2010.
3. Donelli, M., I. Craddock, D. Gibbins, and M. Sarafianou, "A three-dimensional time domain microwave imaging method for breast cancer detection based on an evolutionary algorithm," *Progress In Electromagnetics Research M*, Vol. 18, 179–195, 2011.
4. Kusiak, S. and J. Sylvester, "The scattering support," *Comm. Pure Appl. Math.*, Vol. 56, No. 11, 1525–1548, 2003.
5. Kusiak, S. and J. Sylvester, "The convex scattering support in a background medium," *SIAM J. Math. Anal.*, Vol. 36, No. 4, 1142–1148, 2005.
6. Chiappe, M. and G. L. Gragnani, "An analytical approach to the reconstruction of the radiating currents in inverse electromagnetic scattering," *Microwave and Optical Technology Letters*, Vol. 49, No. 2, 354–360, Feb. 2007.
7. Gragnani, G. L., "Two-dimensional non-radiating currents for imaging systems: Theoretical development and preliminary assessment," *IET Microwaves, Antennas and Propagation*, Vol. 3, No. 8, 1164–1171, Dec. 2009.
8. Li, X. and S. C. Hagness, "A confocal microwave imaging algorithm for breast cancer detection," *IEEE Microw. Wireless Compon. Lett.*, Vol. 11, No. 3, 130–132, Mar. 2001.
9. Lazaro, A., D. Girbau, and R. Villarino, "Simulated and experimental investigation of microwave imaging using UWB," *Progress In Electromagnetics Research*, Vol. 94, 263–280, 2009.
10. Fear, E. C., X. Li, S. C. Hagness, and M. A. Stuchly, "Confocal microwave imaging for breast cancer detection: Localization of tumors in three dimensions," *IEEE Trans. Biomed. Eng.*, Vol. 4, No. 8, 812–822, Aug. 2002.
11. Bond, E. J., X. Li, S. C. Hagness, and B. D. Van Veen, "Microwave imaging via space-time beamforming for early detection of breast cancer," *IEEE Transactions on Antennas and Propagation*, Vol. 51, No. 8, 1690–1705, Aug. 2003.
12. Li, X., S. K. Davis, S. C. Hagness, D. W. Van der Weide, and B. D. Van Veen, "Microwave imaging via space-time beamforming: Experimental investigation of tumor detection in multilayer breast phantoms," *IEEE Transactions on Microwave Theory and Techniques*, Vol. 52, No. 8, 1856–1865, Aug. 2004.
13. Klemm, M., I. J. Craddock, J. A. Leendertz, A. Preece, and R. Benjamin, "Radar-based breast cancer detection using a hemispherical antenna array experimental results," *IEEE Transactions on Antennas and Propagation*, Vol. 57, No. 6, 1692–1704, Jun. 2009.
14. Ghavami, N., G. Tiberi, D. J. Edwards, and A. Monorchio, "UWB microwave imaging of objects with canonical shape," *IEEE Transactions on Antennas and Propagation*, Vol. 60, No. 1, 231–239, Jan. 2012.
15. Tiberi, G., N. Ghavami, D. J. Edwards, and A. Monorchio, "Ultrawideband microwave imaging of cylindrical objects with inclusions," *Microwaves, Antennas & Propagation, IET*, Vol. 5, No. 12, 1440–1446, Sep. 16, 2011.
16. Tiberi, G., N. Ghavami, D. J. Edwards, and A. Monorchio, "Novel techniques for UWB microwave imaging of objects with canonical shape," *PIERS Proceedings*, 808–812, Marrakesh, Morocco, Mar. 20–23, 2011.
17. Stratigaki, L. G., M. P. Ioannidou, and D. P. Chrissoulidis, "Scattering from a dielectric cylinder with multiple eccentric cylindrical dielectric inclusions," *IEE Proceedings — Part H: Microwaves, Antennas and Propagation*, Vol. 143, No. 6, 505–511, Dec. 1996.
18. Ioannidou, M. P., K. D. Kapsalas, and D. P. Chrissoulidis, "Electromagnetic-wave scattering from an eccentrically stratified, dielectric cylinder with multiple, eccentrically stratified, cylindrical, dielectric inclusions," *Journal of Electromagnetic Waves and Applications*, Vol. 18, No. 4, 495–

- 516, 2004.
19. Jarem, J. M., "Rigorous coupled wave analysis of bipolar cylindrical systems: Scattering from inhomogeneous dielectric material, eccentric, composite circular cylinders," *Progress In Electromagnetics Research*, Vol. 43, 181–237, 2003.
 20. Stratton, J. A., *Electromagnetic Theory*, McGraw-Hill Book Company, 1941.
 21. Li, X., S. K. Davis, S. C. Hagness, D. W. Van der Weide, and B. D. Van Veen, "Microwave imaging via space-time beamforming: Experimental investigation of tumor detection in multilayer breast phantoms," *IEEE Trans. Microwave Theory Tech.*, Vol. 52, No. 8, 1856–1865, Aug. 2004.
 22. Gabriel, C., S. Gabriely, and E. Corthout, "The dielectric properties of various tissues," *Phys. Med. Biol.*, Vol. 41, 2231–2249, 1996.
 23. Chen, Y., E. Gunawan, K. S. Low, S. Wang, Y. Kim, and C. B. Soh, "Pulse design for time reversal method as applied to ultrawideband microwave breast cancer detection: A two-dimensional analysis," *IEEE Transactions on Antennas and Propagation*, Vol. 55, No. 1, 194–204, 2007.
 24. Iizuka, K., "An agar-agar chamber for study of electromagnetic waves in an inhomogeneous medium," *IEEE Transactions on Antennas and Propagation*, Vol. 19, No. 3, 365–377, 1971.